Supporting Information

A Novel Soft Actuator for Musculoskeletal System

*Lianjun Wu, Indrajeet Chauhan, and Yonas Tadesse**

Dr. L. Wu, I. Chauhan, Prof. Y. Tadesse
800 W Campbell Rd, Richardson TX, 75080, USA
E-mail: yonas.tadesse@utdallas.edu

Materials and Methods:

1. Muscular System: Muscle Fabrication Procedure

Based on the fabrication method, twisted and coiled polymer (TCP) muscles can be characterized into two types, namely self-coiled and mandrel-coiled. Whereas self-coiled muscles are those that coil themselves due to extreme twisting, mandrel-coiled muscles are those that are coiled over a core rod after twist insertion. TCP muscles from sewing thread are categorized as self-coiled muscles and the details of producing the artificial muscles can be found in literature.[1,2] Artificial muscles produced from sewing thread with conductive silver coating have been widely used for different applications due to the ease of delivering heat to muscles via electro-thermal heating. Some of the demonstrated applications of TCP muscles are found in robotic hand/prosthetic hand,[2-4] orthotic device,[5,6] sensors,[7,8] musculoskeletal system,[9,10] healing composites,[11] energy harvester[12] and tensegrity robot.[13] Even though TCP muscles made from sewing thread are easy to actuate due to electro-thermal heating, the silver coating, which facilitates electric conduction and Joule heating, drives up the cost of the precursor material. On the other hand, while fishing line muscles are cost efficient, the precursor material is not manufactured with a conductive coating. Therefore, a resistance wire can be added together with fishing line to produce artificial muscle. For this reason, a novel apparatus is developed to create mandrel-coiled artificial muscle from fishing line wrapped with a heating wire. The manufacturing technology proposed in this

section enables researchers to easily fabricate muscles having identical and repeatable characteristics.

The muscle proposed in the paper consists of a nylon 6 monofilament as the precursor material (860 μm diameter Eagle Claw monofilament fishing fine) and nickel chromium wire with 80 μm diameter (Stock number: 8880K87 from McMaster.com) as the heating element. Using the nickel-chromium wire to heat the fishing line muscle requires uniform and extensive surface contact between the fishing line and heating wire. At the same time, since the nichrome wire has its own stiffness, wrapping the wire too densely to ensure extensive surface contact may compromise the dynamic properties of the fishing line itself. This challenge can be addressed by wrapping a very thin nickel-chromium wire around the precursor material in a small pitch at a constant speed. The easy-to-form nickel chromium alloy wire acts like a soft bend-and-stay wire so that it can provide a conformal conductive layer without affecting the actuation of the muscle. The home-made experimental setup in **Figure S1** is made of commercially available electronic and mechanical components, which enables others to replicate and use the device easily. The setup consists of 3 stepper motors, one linear motion slide, and a carriage, attached to the linear motion slide, which guides the wrapping of the heating wire.

1.1 Twist Insertion

For fabricating the muscles, a certain length of fishing line needs to be cut to fit the traveling range of the linear motion slide. For our setup, a 145-cm long fishing line was used. One end of the fishing line was attached to the top stepper motor (MT1) using a safety pin, while the other end was suspended with a 500-gram load to keep the fiber under tension. Besides the load, a stopper was also placed at the bottom of the deadweight to prevent the fiber from untwisting. Subsequently, the motor was turned on to rotate in the direction in which the right-hand fingers curl when the

right thumb points upwards, and the fiber was allowed to twist. During this process of twist insertion, the load moved up as the fiber twisted and shrunk in length. The motor was stopped, and the process ended when the first coil formed along the fiber.

1.2 Incorporation of the Resistance Wire

The next step is to incorporate the heating wire into the muscle by wrapping the nichrome around the twisted fiber as shown in **Figure 1SA**. In this step, the stopper used in the previous step was removed, and a new untwisted precursor fishing line fiber was attached to the bottom of the twisted fishing line fiber. The 500-gram load was released from the twisted fiber and attached to the bottom of the new untwisted fiber. The length of the new untwisted fiber was determined such that the attached load would be in contact with the ground to not only prevent the twisted fiber from untwisting, but to also enable the rotation of the twisted fiber to wrap the heating wire around the fiber. After suspending the weight from the new untwisted fiber, the carriage on the linear motion slide driven by MT2 was moved to the starting position or towards MT1. Next, one end of the heating wire was attached to MT1, while the rest of the wire was routed around a guide rod. The resistance wire pool was placed on the pool holder, and a 20-gram load was hung on the heating wire to keep it taut during the wrapping process and provide a uniform and constant wrapping angle. MT1 was rotated following previous direction and the carriage on the linear motion slide started to move downwards slowly at a constant speed, thereby creating a uniform wrapping of the heating wire around the twisted fiber. The pitch in the wrapped heating wire could be adjusted by controlling the rotating speed of the top MT1 and bottom MT2.

1.3 Mandrel Coiling

The third step is to wrap the twisted fiber with heating wire around a mandrel as shown in **Figure 1SB**. After incorporating the nichrome wire, the weight at one end of the fiber was maintained, and the safety pin attached to the other end of the fiber was passed through a hole in a locker located at the end of the mandrel close to MT3 so that the twisted fiber was firmly attached to the rod. Once the muscle was fixed at one end of the rod, the motor (MT3) was turned on to allow the twisted fiber to wrap or coil around the mandrel. In this step, the rotating direction of MT3 determined whether the fabricated muscle contracted or expanded. If MT3 rotated in the same direction as the direction of twist, then the muscle would contract along the lengthwise direction when heated. On the contrary, if MT3 rotated in the opposite direction, the muscle would expand along the lengthwise direction. Additionally, in this step, the diameter of the rod determined the spring index of the muscle. Therefore, by changing the diameter of the rod, muscles of different diameters and spring indices could be created.

1.4 Thermal Annealing

The final step is to retain the shape of the muscle by annealing the muscle in a furnace. After the twisted fiber with the nichrome wire was uniformly wrapped or coiled along the rod, the rod was detached from MT3 and placed in an aluminum frame which held the rod by the ends. To prevent the unwrapping of the fiber, two clamps were used to fix both ends of the muscle. The furnace was preheated to 180℃ and the whole frame was kept in the furnace for one and a half hours. The annealing temperature for nylon 6 monofilament fishing line was 180℃. However, in general, this temperature depends on the chosen fiber, and is usually set to be above the maximum actuation temperature, but below the melting point.

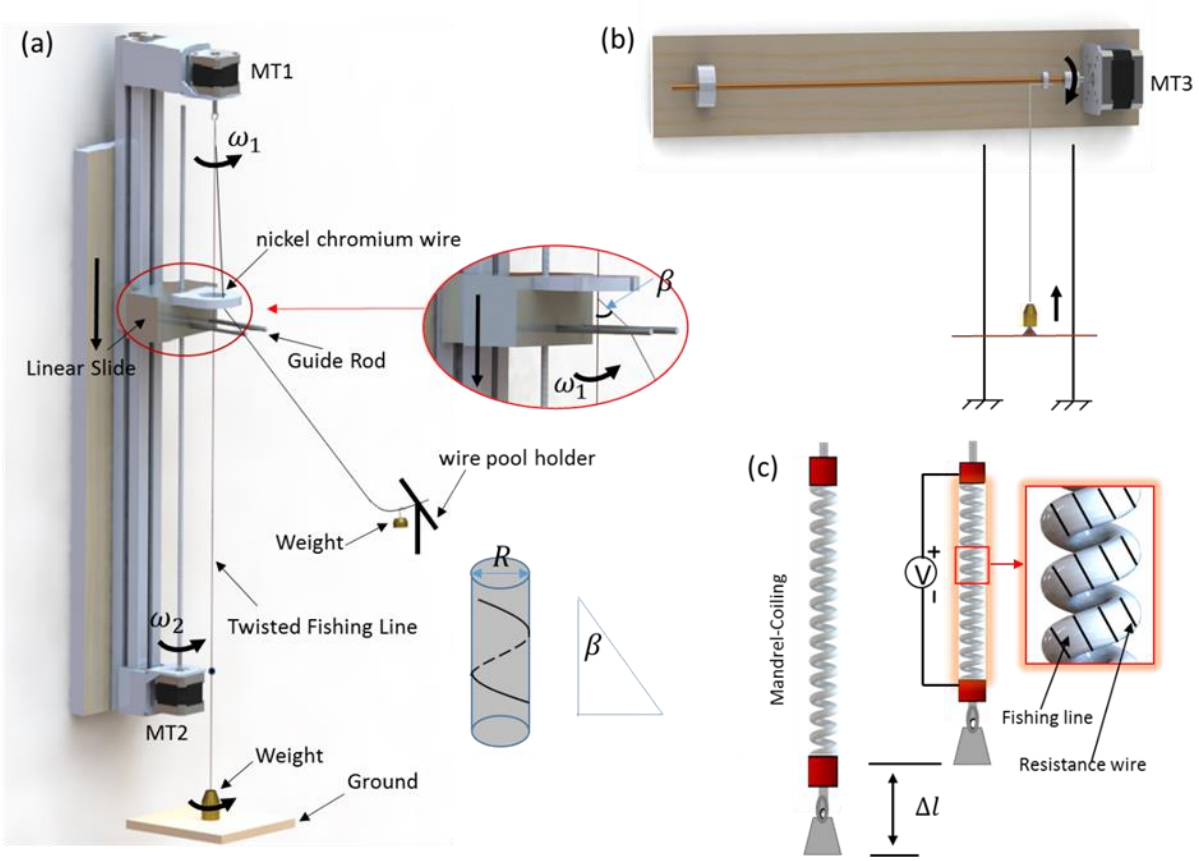

Figure 1S: Schematic diagram of the developed Fishing line TCP muscle fabrication. (a) Incorporating the nickel chromium wire (resistance wire) into the muscle by wrapping the resistance wire around the twisted fiber. (b) Forming the mandrel-coiling muscle from the twisted fiber with resistance wire as made in (a) by wrapping it around the rod via the rotation of the stepper motor. (c) The working principle of the fishing line TCP muscle with resistance wire; Left of (c) the muscle at rest when hanging a weight to the bottom; Right of (c) the muscle contracts upon receiving Joule heat.

2. Skeletal System: Ball-and-Socket Joint

The CAD designs for the mold and the skeletal structures were created in SolidWorks, and the ball-and-socket joint assembly was 3D printed with ABS-plus material using Stratasys Fortus 250MC. Novus plastic clean & shine and Novus fine scratch remover were used to clean the surface of printed parts to get a fine surface. To mimic the synovium's fluid and provide lubrication, jet-lube grease was added into the clearance between the ball and the socket parts. Finally, to replicate the capsule, silicone elastomer (Ecoflex® 00-10 shore hardness) was used to fabricate

the stabilizing element. The ABS printed joint allows for the movement of the system through the contraction of the antagonistic pair of muscles.

3. Joint stiffness and Muscle Stiffness

In order to determine how much force and contraction is required to achieve the maximum bending angle, we characterized the force versus contraction of the joint structure using the experimental setup as shown in **Figure 2Sa**. The setup consisted of a load cell (Futek LSB200), a laser displacement sensor (Keyence LK-G152), a power supply (BK Precision 1687B), a National Instrument DAQ, and home-made motorized linear stage. Within the NI DAQ, data was acquired using the NI 9219, NI 9201, and NI 9221 modules. Specifically, the NI 9219 module was used to record temperature at a rate of 50 S/s, and displacement and force at 100 S/s, whereas the NI 9201 and the NI 9221 modules were used to acquire the current and voltage at 500 kS/s and 800 kS/s respectively. For the experiment, the base of the sample joint structure was secured to a fixture, and an inextensible string was attached to the other base of the joint through the hollow channel. The linear stage was driven at a constant speed of 0.12 mm/s until the traveling distance reached 7 mm, which was found to be sufficient to bend the joint to the maximum bending angle. Because the distance between the bases of the joint was 47 mm to accommodate the muscle, the actuation stroke required for the muscle was at least 14.9% (7 mm/47 mm) when loaded with a spring.

In this study, 3 different prototypes with similar structures were fabricated. While prototype 1 and prototype 2 had the same volume of silicone in the stabilization element, their side hollow channels had different thicknesses. On the other hand, Prototype 2 and Prototype 3 had the same channel thickness, but different volumes of silicone in the stabilization element. Prototype 2 was modified from prototype 1 by reducing the thickness of the channel from 1.5 mm to 0.9mm, and prototype 3 was modified from prototype 2 by reducing 15% of the silicone volume in the

silicone ligament (stabilization element). Another experimental setup as shown in **Figure 2SB** is designed to measure the stiffness behavior of the fabricated muscle.

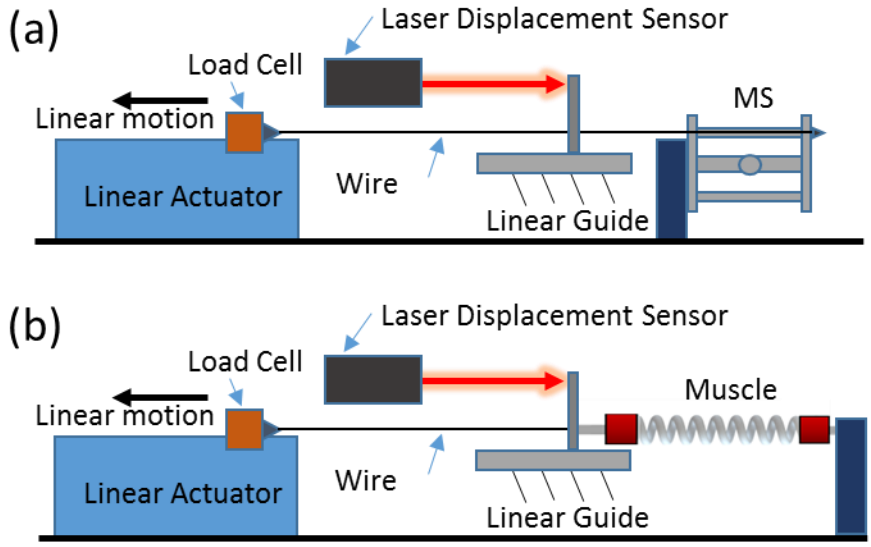

Figure 2S: Schematic diagram of the experimental setup to characterize the stiffness of the joint (a) and muscle (b). ~~(c)~~ The measurement of force during stiffness test; Prototype 2 was modified from prototype 1 by reducing the thickness of the channel from 1.5 mm to 0.9mm, and prototype 3 was modified from prototype 2 by reducing 15% of the silicone volume in the silicone ligament.

4. Muscle Characterization

The experimental setups as shown in **Figure 3S** were used to characterize the performance of TCP_{NC}^{FL} muscle as an actuator. **Figure 3Sa** shows the schematic diagram of the setup used in isotonic tests (constant load) and **Figure 3Sb** shows the muscle works against a linear spring (spring load). We selected a linear spring with a stiffness of 133N/m considering the comparable stiffness of 125 N/m for the muscle and the joint combined. The lengthwise contraction displacement was measured via a laser displacement sensor (Keyence LK-G152), the pulling force was measured via a load cell (Futek LSB200), and the temperature was obtained by a type-E thermocouple. The power input waveforms were programmed and defined in a power supply (BK Precision 1687B) and current was set as a constant value. All the state variables of TCP_{NC}^{FL} Muscle including pulling force, voltage, displacement and temperature were measured synchronously and

stored in the master PC. Here and elsewhere, tensile actuation was calculated as the ratio of the amount of contraction to the loaded length of the muscle. Pre-tension was varied by translating the linear stage in discrete steps.

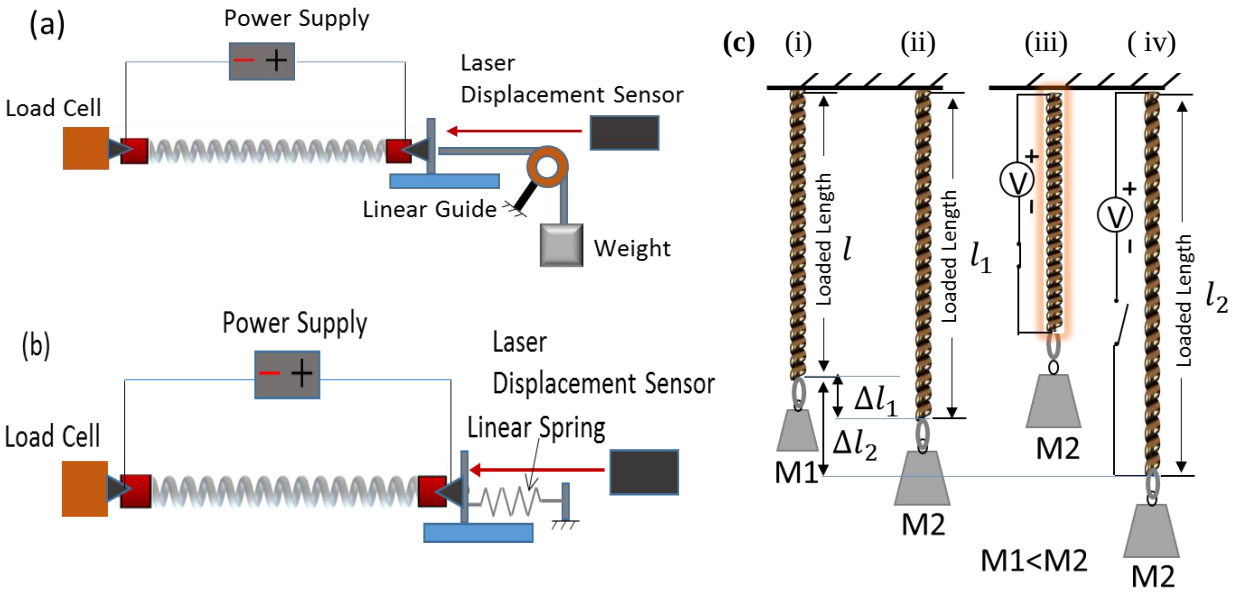

Figure 3S. (a) Schematic diagram of the experimental setup for characterization of the Fishing Line TCP muscle in isotonic test. (b) Schematic diagram of the experimental setup for characterization of the Fishing Line TCP muscle in spring-load test. (c) muscle length under load and actuation.

4.1 Stiffness variation of the muscle under different test conditions

The stiffness of the TCP muscles is measured under two different conditions. The first one is stiffness measurement via tensile test (no heating and no actuation) using experimental setup in **Figure 2Sb.** The other stiffness is estimated via isotonic test (actuated state and heated) based on the loaded length vs corresponding load using the experimental setup (**Figure 3Sa**) and the loaded length is measured after training and actuation at each corresponding load. Training and actuation affect the length of the muscles. **Figure S3c** can better explain the difference. In the tensile test, the process is similar to that from (i) to (ii), and no heating occurs; By increasing the load from M1 to M2, the loaded length is increased from l to l_1. The elongation is Δl_1. In the isotonic test,

the process is similar to that from Figure (i) to (iv), and due to the training and actuation in Figure (iii), the loaded length is further increased from l_1 to l_2. The total elongation is Δl_2. Since the elongation in isotonic test at a certain load is larger than that in tensile test at the same load, the stiffness measured (49 N/m) in isotonic test in Figure 3A is less than that (85 N/m) measured in tensile test in Figure 2H.

4.2 Isotonic Test Results

Figure 4S shows all the time domain state variables of the TCP_{NC}^{FL} muscle and the results are highly repeatable and consistent. Due to the friction induced by the pulley, some fluctuations in the measured force were observed in **Figure 4Sa**, but the force magnitudes were nearly constant during the actuation period. In **Figure 4Sb**, significant changes in the measured voltage were mainly because the neighboring coils, stretched under a low load condition, were in close contact during actuation such that the resistance wire between the coils interacted with itself, resulting in the decrease in resistance. The point at which the voltage drops reflects the time when the coils start contacting. The maximum power consumption of the muscle is 1.6W.

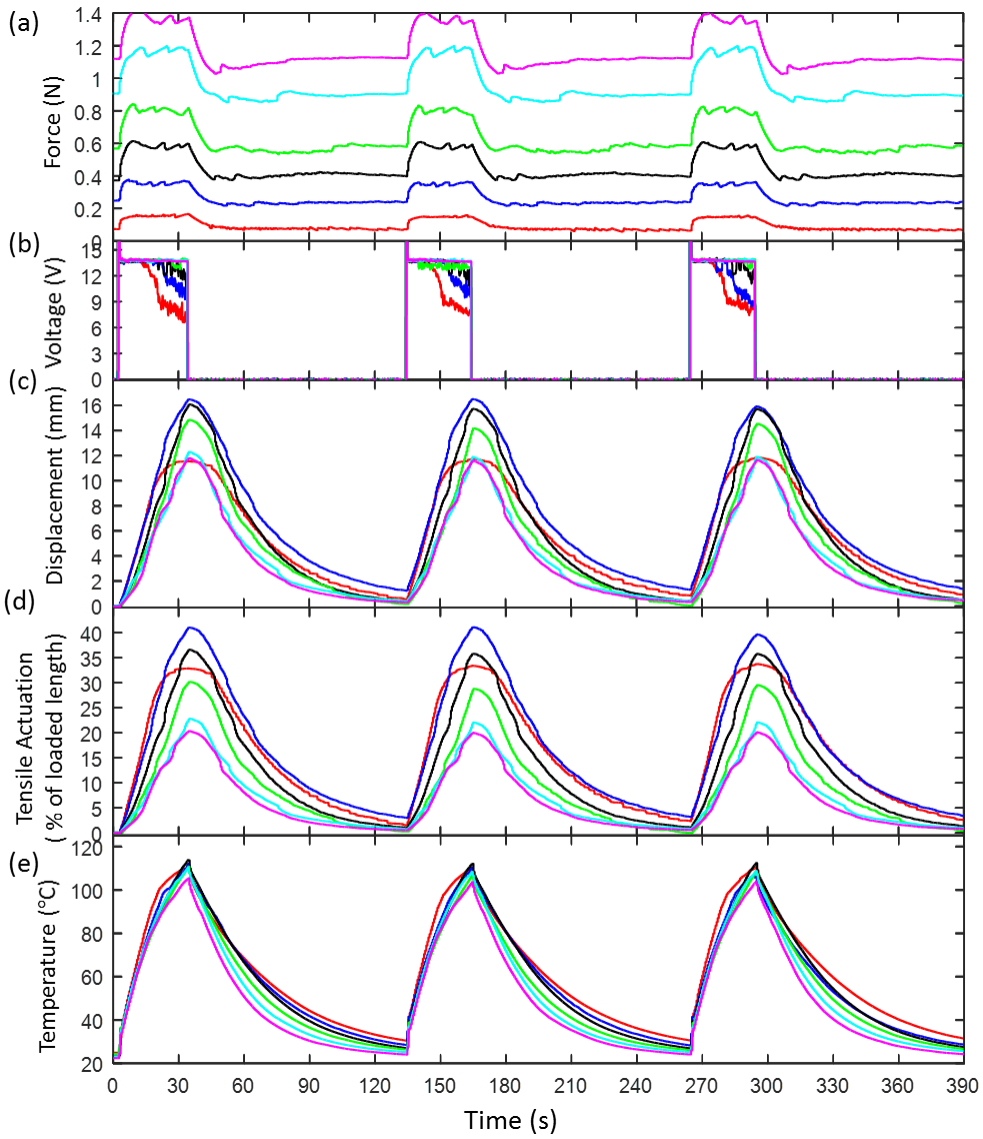

Figure 4S. Mechanical response in an isotonic test of a fishing line TCP muscle fabricated from an 860-um-diameter nylon 6 monofilament that was mandrel coiled incorporating an 80-um-diameter resistance wire, which resulted in spring index of 5.2: (a) the measured force profile, (b) the measured voltage profile, (c) the measured absolute displacement profile, (d) tensile actuation stroke, as a percent of the loaded muscle length, (e) the measured temperature profile characteristics measured at different pre-tension levels,

4.3 Spring-load Test

In **Figure 5Sb**, as the current was kept constant in all the experiments, the voltage magnitudes measured between the muscle's terminals in the first few seconds were the same until the neighboring resistance wire started contacting, which resulted in the fluctuation of voltage. The

maximum percentage of contraction was 15% and the maximum temperature was ~110^{0}C (**Figure 5Sd** and **e**). At pre-tensions greater than 0.31N, the temperature remained almost the same mainly due to the supplied constant current, whereas the temperature at pre-tension 0.11N was higher than the rest, which may result from the accumulated heat in local region because of the compact spacing between the neighboring coils at low pre-tension.

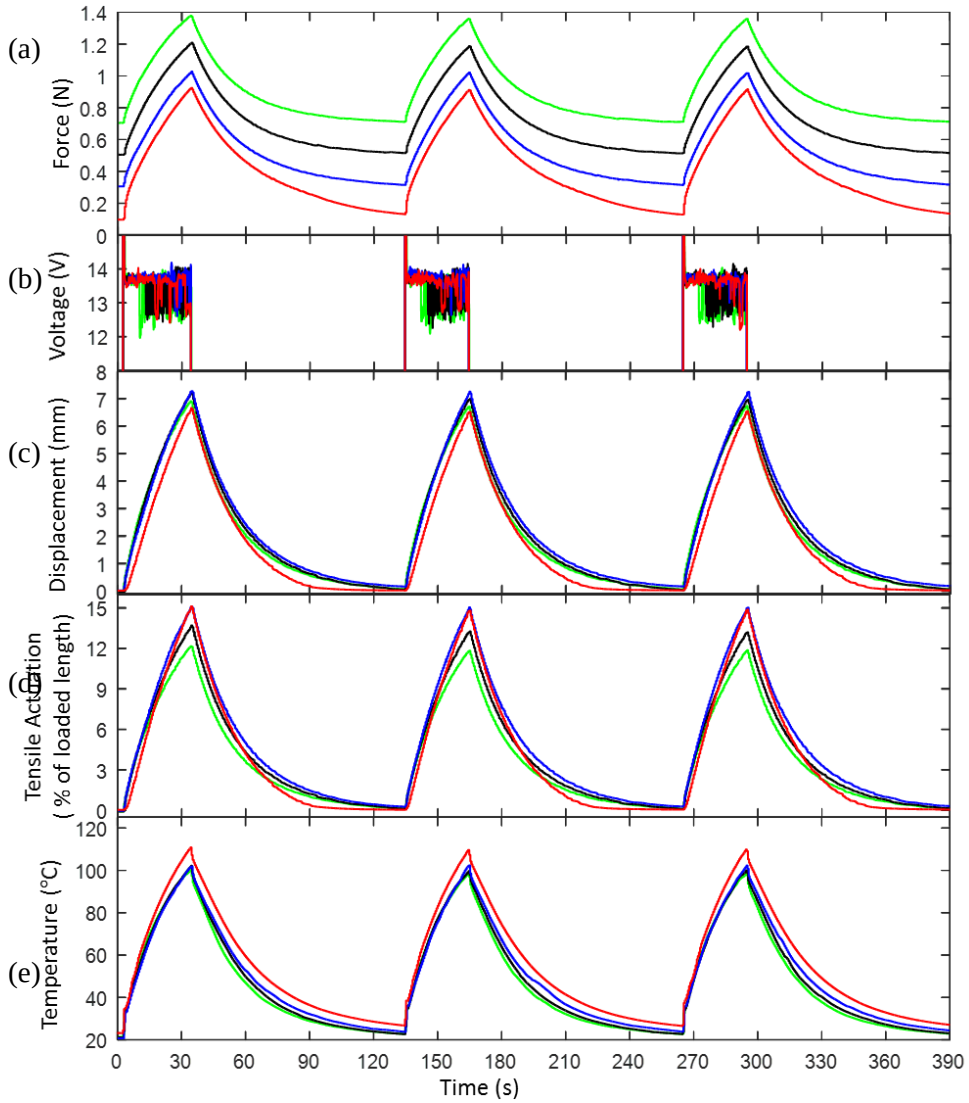

Figure 5S. Mechanical response of a fishing line TCP muscle fabricated from an 860-um-diameter nylon 6 monofilament that was mandrel coiled incorporating an 80-um-diameter resistance wire, which resulted in spring index of 5.2, against a passive spring of stiffness of 133 N m^{-1} under different pre-tension: (a) the measured force profile, (b) the measured voltage profile, (c) the measured absolute displacement profile, (d) tensile actuation stroke, as a percent of the loaded muscle length, and (e) the measured temperature profile characteristics measured at different pre-tension levels.

4.4 Pulsed Actuation

The experimental setup used for the measurement of tensile actuation and pulling force here was also the same as shown earlier in **Figure 3Sb**. The test was carried out by varying the high current pulse magnitude at 0.42 A, 0.46A and 0.50A for a short duration of 1s for all pulsed tests.

4.5 Endurance test

Preliminary life cycle test was conducted on a muscle (length 50 mm). The displacement was measured using the laser displacement sensor. The result of the endurance test is shown in **Figure 6S.** The muscle was driven by a pulsed current 0.5A (duty cycle 1%, a period of 101 s) continuously under a constant 50-gram load for a total 2300 cycles in ambient air. The result shows a slight degradation in performance.

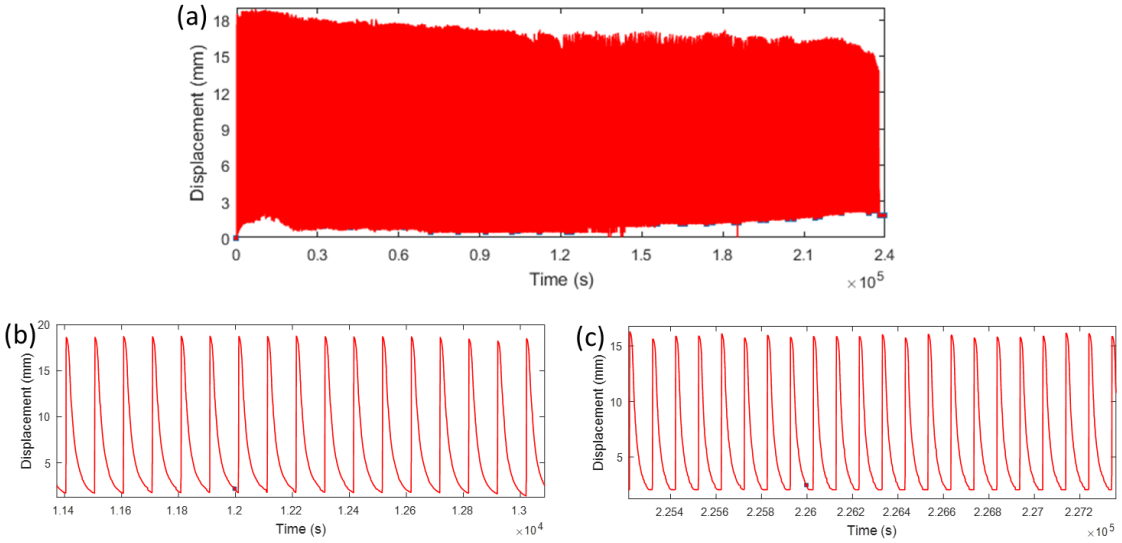

Figure 6S. Endurance test of the artificial muscle under a 50-gram load (a) where 1s pulsed power cycle and 100s cooling cycle with a magnified views (b) and (c).

5. Musculoskeletal System Characterization

Before the muscles were integrated into the joint, they were trained with a dead weight of 100 grams at a current of 0.14 A for at least 4 cycles or until the actuation results were repeatable for 4 consecutive cycles. Each cycle consisted of 30 s for actuation and 100 s for relaxation. The training was performed using the experimental setup in **Figure 3Sa.** The purpose of this training was to achieve consistency in stiffness, length, and actuation of the muscles at constant load. After the muscles were placed into the joint, they were then trained again for repeatability in a spring load setting. Subsequently, the base of the joint was fixed on a 3D printed support, and regular actuation and pulse actuation tests, which differed in terms of cycle frequency and current magnitudes, were performed. The regular actuation test was similar to the training cycle, i.e. it consisted of 30 s for actuation and 100 s for relaxation. For the pulse actuation tests, the actuation time was set to 1 s and the appropriate current was determined experimentally. A safe and optimum current was found to be 0.50 A, while the maximum current, which could break the muscle, was approximately 0.57A. To explore the effect of change in current on the actuation, three different currents ranging from 0.42 A to 0.50 A at an increment of 0.04 A were provided. Similar to other tests, pulsed actuation cycles were repeated at least 3 times to determine repeatability. All the angular displacement plots were obtained using an open source physics software called Tracker. Pictures of the musculoskeletal system in the pulsed test (1 s for actuation and 30 for relaxation) are shown in **Figure 7S.**

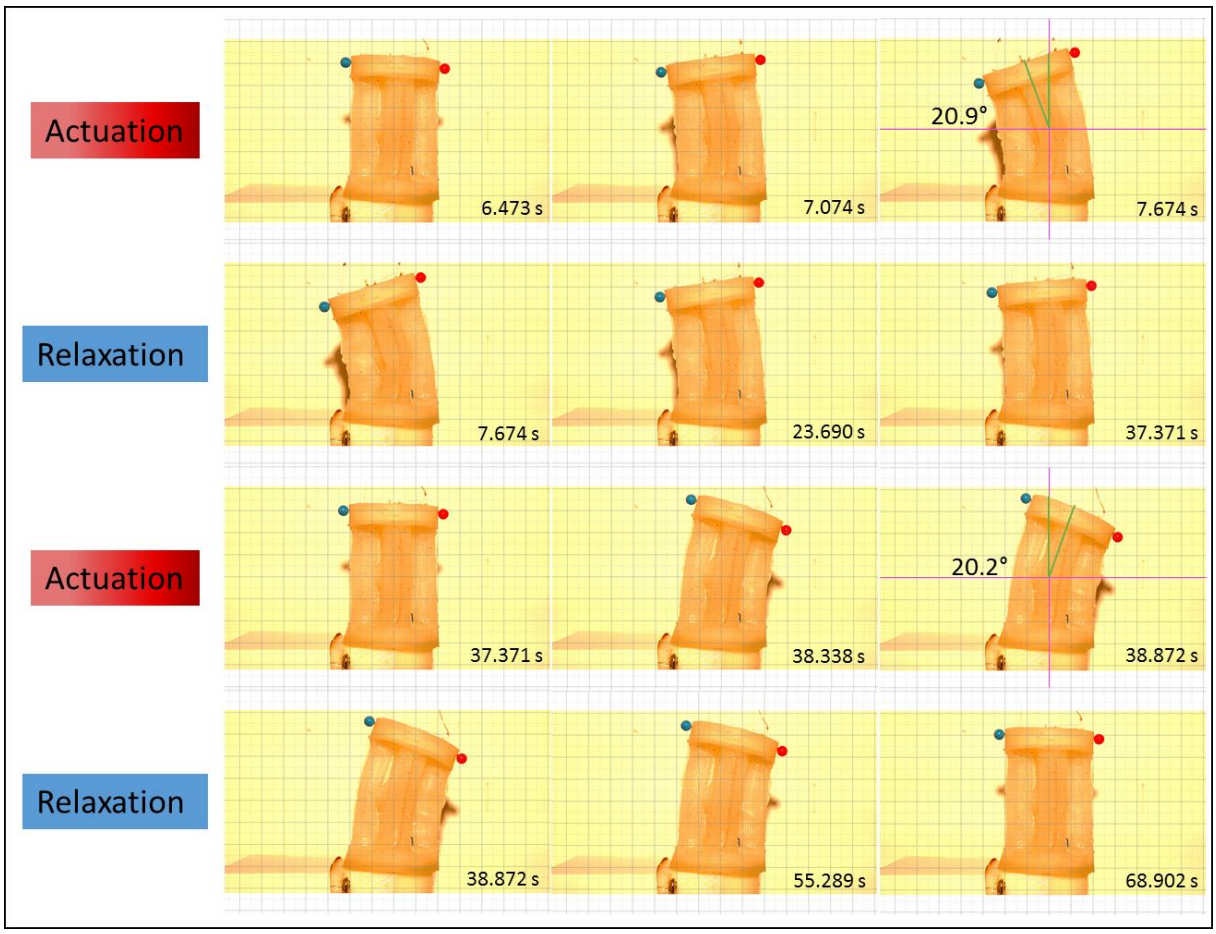

Figure 7S. The bending motion of the musculoskeletal system.

6. Position Analysis of MS

In the MS, the performance of the artificial muscle determines the working space of the final prototype of the MS joint. The purpose of position analysis is to investigate the relationship between the pose of the top moving plate and the muscle tensile actuation. The kinematic diagram of the MS joint is shown in **Figure 8S**. Coordinate system 1 and coordinate system 2 are attached to the base and moving plate, respectively. The origins of both these coordinate systems are located at the center of the ball-and-socket joint, and both coordinate systems coincide with each other in the initial position where no muscle is actuated. The orientation of coordinate system 1 with respect to coordinate system 2 can be described by the rotation matrix $R \in SO(3)$. The orientation of MS

can also be described by XYZ Euler angles, i.e., θ_1, θ_2, and θ_3, where θ_1 is the angular displacement about the X axis of the coordinate system 1, θ_2 is the angular displacement about the Y axis of the previously rotated coordinate system, and θ_3 is 0 since in our case there is no rotation about the Z axis. In this case, the transformation matrix ${}^1_2R$ can be represented by the following formula:

$$ {}^1_2R=\begin{bmatrix}1 & 0 & 0\\ 0 & \cos\theta_1 & -\sin\theta_1\\ 0 & \sin\theta_1 & \cos\theta_1\end{bmatrix}\begin{bmatrix}\cos\theta_2 & 0 & \sin\theta_2\\ 0 & 1 & 0\\ -\sin\theta_2 & 0 & \cos\theta_2\end{bmatrix}\begin{bmatrix}1 & 0 & 0\\ 0 & 1 & 0\\ 0 & 0 & 1\end{bmatrix} \quad \text{(S1)} $$

Expanding (S1) gives

$$ {}^1_2R=\begin{bmatrix}c\theta_2 & 0 & s\theta_2\\ s\theta_1 s\theta_2 & c\theta_1 & -s\theta_1 c\theta_2\\ -c\theta_1 s\theta_2 & s\theta_1 & c\theta_1 c\theta_2\end{bmatrix} \quad \text{(S2)} $$

Where $c\theta_i$ and $s\theta_i$ represent the cosine and sine of θ_i $(i = 1,2)$.

Vector ${}^1\mathrm{OP}$ (P=A, B, C, D) denotes the position vector of the four-muscle's attachment point on the base in the coordinate system 1. Vector ${}^2\mathrm{Op}$ (p=a, b, c, d) denotes the position vector of the four-muscle's attachment point on the base in the coordinate system 2. For the given orientation angles referring to the Figure 7S, according to the vector loop-closure equation, the analytical expressions for the artificial muscle length ${}^1\mathrm{Pp}$, (${}^1\mathrm{Aa}$, ${}^1\mathrm{Bb}$, ${}^1\mathrm{Cc}$, and ${}^1\mathrm{Dd}$) can be written as:

$$ {}^1\mathrm{Pp} = {}^1_2R\ {}^2\mathrm{Op} - {}^1\mathrm{OP} \quad \text{(S3)} $$

Note that the coordinates of the muscle attachment points on the base and moving plate are expressed as:

$$ \begin{aligned} {}^1\mathrm{OA} &= [r \quad 0 \quad -h]^{\mathrm{T}} & {}^2\mathrm{Oa} &= [r \quad 0 \quad h]^{\mathrm{T}}\\ {}^1\mathrm{OB} &= [0 \quad r \quad -h]^{\mathrm{T}} & {}^1\mathrm{Ob} &= [0 \quad r \quad h]^{\mathrm{T}}\\ {}^1\mathrm{OC} &= [-r \quad 0 \quad -h]^{\mathrm{T}} & {}^1\mathrm{Oc} &= [-r \quad 0 \quad h]^{\mathrm{T}}\\ {}^1\mathrm{OD} &= [0 \quad -r \quad -h]^{\mathrm{T}} & {}^1\mathrm{Od} &= [0 \quad -r \quad h]^{\mathrm{T}} \end{aligned} \quad \text{(S4)} $$

Equation (S3) can be rewritten as follows:

$$ ({}^1\mathrm{Pp})^2 = ({}^1_2R\ {}^2\mathrm{Op} - {}^1\mathrm{OP})^2 \quad \text{(S5)} $$

Equation (S5) can be further rearranged in the following form:

$$ ({}^1\mathrm{Pp})^2 = ({}^1\mathrm{Op})^2 + ({}^1\mathrm{OP})^2 - 2\,{}^1\mathrm{OP}^{\mathrm{T}}\,{}^1_2R\ {}^2\mathrm{Op} \quad \text{(S6)} $$

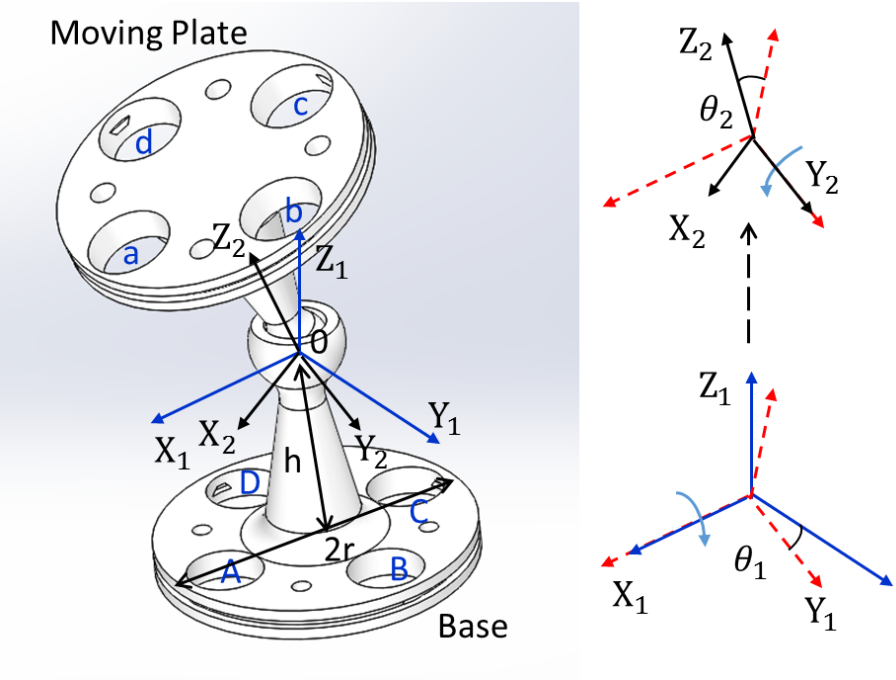

Figure 8S. Position diagram of the MS.

7. Temperature distribution along the actuator

To observe the temperature distribution, thermal imaging of the muscle was performed using FLIR camera (TG165, FLIR® Systems, Inc.). First the camera was mounted at a distance of 30 mm from the surface of the muscle as shown in Figure 9S. Next, the emissivity was adjusted by comparing the maximum temperature reading from thermocouple and IR camera. We found out that the temperature reading matches when the emissivity is set to 0.22 at higher temperature above ~80 ^{0}C. At lower temperature range below 50 ^{0}C, the reading from IR camera was less than that from thermocouple. The IR images corresponding to the temperature changes at the input current 0.12 A during heating. There is a slight difference in the temperature distribution along the surface. At low temperature (27 ^{0}C) the temperature is more uniformly distributed along the axial direction compared to high temperature (90 ^{0}C).

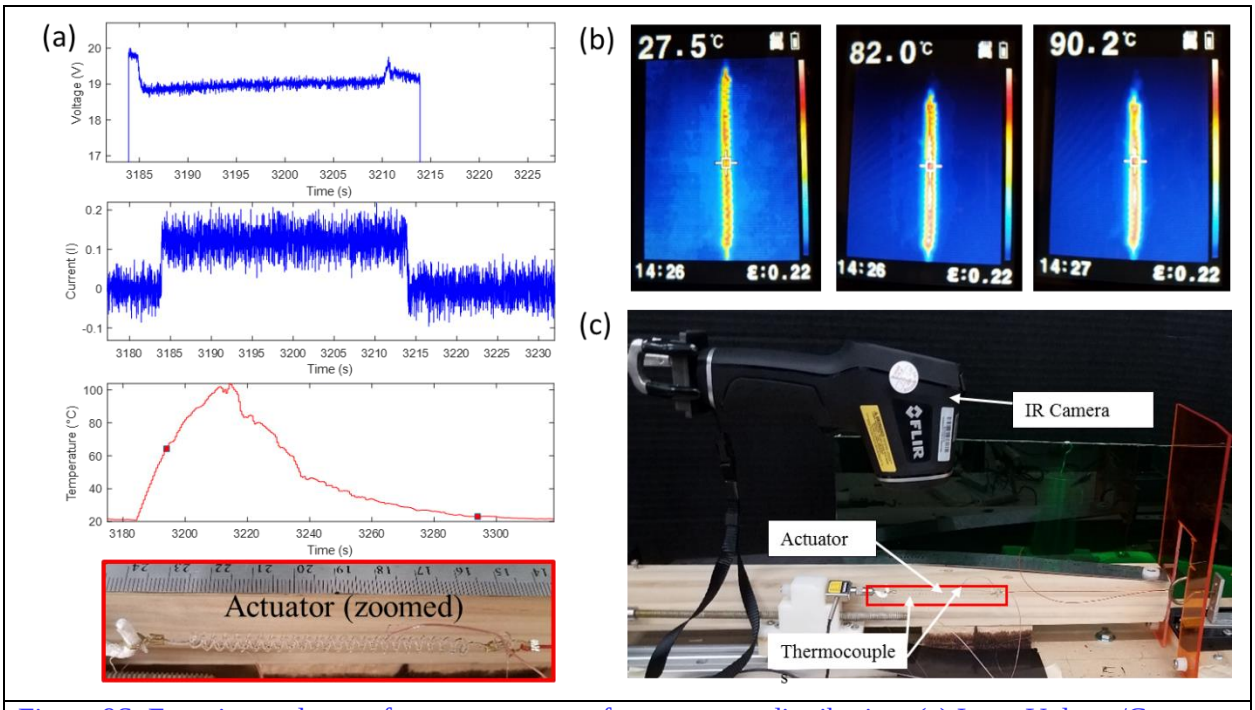

Figure 9S. Experimental setup for measurement of temperature distribution. (a) Input Voltage/Current and Temperature measured using thermocouple; (b) Infrared images; and (c) experimental setup.

8. Time constant determination

The heating and the cooling curves can be estimated using a lumped parameter model and constant resistance which works well for similar actuators, such as shape memory alloy (SMA).[14] This model can be expressed by the following equation.

$$mc_p \frac{dT}{dt} = \left\{ \frac{V^2}{R} - hA_c(T - T_\infty) \right\} \qquad \text{(S7)}$$

Where m is the mass, c_p is the specific heat capacity, h is the convective heat transfer coefficient, A_c is the surface area of the muscle, V is the voltage, R is the resistance, and T_∞ is the ambient temperature.

Equation (S7) can determine both the cooling and the heating curves.

When there is no power $(\frac{V^2}{R} = 0)$ for the cooling stage, the heating part of equation (S7) is removed and the solution of equation (S7) can be written as

$$T(t) = T_\infty + (T_0 - T_\infty)e^{-\tau t} \quad \text{(S8)}$$

The time constant $\tau = \frac{hA_c}{mc_p}$ is dependent on the four parameters, surface area of the actuator, convective heat transfer, mass of the actuator, and the specific heat capacity of the actuator. Equation (S8) was used to extract the information. The cooling time constant was reported in Figure 4.

9. Bending Angle and Actuation relationship

There is a specific geometrical relationship referring the following schematic diagram of MS bending motion which can correlate the muscle tensile actuation and the bending angle of the MS.[9]

The geometrical relationship can be expressed using the following equation,

$$(1 - \varepsilon)\cos\theta = \sin\alpha \quad \text{(S9)}$$

Where ε is the muscle tensile actuation, θ is the angle pointing to the muscle attachment from the center of the ball joint, β is the maximum bending angle of the joint and $\alpha = 90 - \theta - \beta/2$.

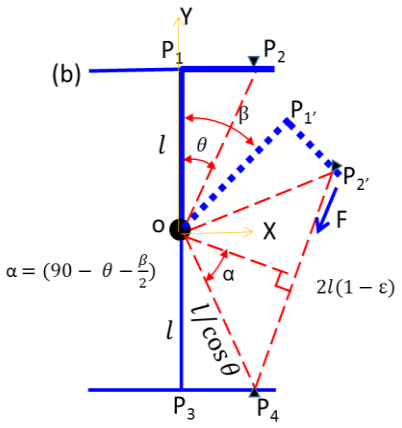

Figure 10S. schematic diagram of MS bending motion

In the current design of MS, $\theta = 28°$. From Figure 5B and Figure 5C, the maximum bending angle $\beta = 25°$ is obtained at the current 0.50 A. Using equation (S9), we can obtain the muscle actuation

$\varepsilon = 11\%$, which is very close to the tensile actuation 12 % reported in Figure 4C at the case of current 0.50 A. From Figure 5A, the maximum bending angle $\beta = 25°$ is obtained at the current 0.14 A. Using equation (S9), we can obtain the muscle tensile actuation $\varepsilon = 14\%$, which is very close to the tensile 15 % reported in Figure 4B at the case of pre-tension 0.12 N. Therefore, we can conclude that the results are nearly consistent.

10. Ball and Socket Joints in Animals

Table S1: Ball and socket joints in human and other animals: range of motion and speed of joints

	Range of motion (RoM, degree)	**Speed of motion [Deg/sec] / frequency[Hz]**
Human shoulder [15,16]	Flexion:180 Extension: 50 Adduction: 0 Abduction: 180.[15]	The maximum speed of a human shoulder during ball throwing could exceed 9000°/sec , which is equivalent to 25 Hz.[16]
Dog[17,18]	Flexion :60-70 Extension: 65-75 Adduction: 40-50 Abduction: 40-50.[17]	Maximum frequency of a dog walking :10 Hz.[18]
Cat [17]	Flexion :60-70 Extension: 90 Adduction: 20-30 Abduction: 80-90	-
Cheetah[18,19]	Spine –Hip :145 Knee :104 Ankle: 95	Max angular velocity of Spine-Hip of a cheetah: 2206 deg/s; knee :2300 deg/s (6.4Hz) ; Ankle : 1763 deg/s.[19] Cheetah can run 61 mph,(27 m/s).[20]
Birds[21]	Three different bird species (oystercatchers, lapwings and avocets) Hip motion: 0-150 Maximum excursion angle of the thigh: 0-60	Maximum velocity of the thighs : 1500 deg/s (4 Hz).[21]
Human Neck(spine)[22-24]	Flexion /Extension: 24-109(M); 37-114 (F) Lateral bending: 26-81(M); 22-75(F) Axial rotation: 90-200(M); 80-170(F) Occ-C1: 2-30 M= Male C1-C2: 2-28 C2-C3: 2-22 F= Female	The maximum speed 382 deg/sec (1 Hz).[23] Rolling: 44^0, Yawing :69^0 Pitching: 110^0

	C3-C4: 2-35 C4-C5: 2-32 C5-C6: 2-36 C6-C7: 2-30 Motion range obtained from 70 subjects.[22]	

Reference

[1] C. S. Haines, M. D. Lima, N. Li, G. M. Spinks, J. Foroughi, J. D. Madden, S. H. Kim, S. Fang, M. J. de Andrade, F. Göktepe, *Science* **2014**, 343, 868.

[2] L. Wu, M. J. de Andrade, L. K. Saharan, R. S. Rome, R. H. Baughman, Y. Tadesse, *Bioinspiration & Biomimetics* **2017**, 12, 026004.

[3] M. C. Yip, G. Niemeyer, presented at Robotics and Automation (ICRA), 2015 IEEE International Conference on **2015**.

[4] A. Arjun, L. Saharan, Y. Tadesse, presented at Automation Science and Engineering (CASE), 2016 IEEE International Conference on **2016**.

[5] L. Saharan, A. Sharma, M. J. de Andrade, R. H. Baughman, Y. Tadesse, presented at SPIE Smart Structures and Materials+ Nondestructive Evaluation and Health Monitoring **2017**.

[6] L. Saharan, M. J. de Andrade, W. Saleem, R. H. Baughman, Y. Tadesse, *Smart Materials and Structures* **2017**.

[7] J. Zhao, A. Abbas, presented at ASME 2016 Dynamic Systems and Control Conference **2016**.

[8] J. van der Weijde, B. Smit, M. Fritschi, C. van de Kamp, H. Vallery, *IEEE/ASME Transactions on Mechatronics* **2017**, 22, 1268.

[9] L. Wu, Y. Tadesse, presented at ASME 2016 International Mechanical Engineering Congress and Exposition **2016**.

[10] Y. Tadesse, L. Wu, L. K. Saharan, *Mechanical Engineering* **2016**, 138, S11.

[11] P. Zhang, G. Li, *Polymer* **2015**, 64, 29.

[12] S. H. Kim, M. D. Lima, M. E. Kozlov, C. S. Haines, G. M. Spinks, S. Aziz, C. Choi, H. J. Sim, X. Wang, H. Lu, *Energy & Environmental Science* **2015**, 8, 3336.

[13] L. Wu, M. J. de Andrade, T. Brahme, Y. Tadesse, R. H. Baughman, presented at SPIE Smart Structures and Materials+ Nondestructive Evaluation and Health Monitoring **2016**.

[14] Y. Tadesse, D. Hong, S. Priya, *Journal of Mechanisms and Robotics* **2011**, 3, 011008.

[15] S. Ikemoto, Y. Kimoto, K. Hosoda, *Bioinspiration & biomimetics* **2015**, 10, 066009.

[16] N. T. Roach, M. Venkadesan, M. J. Rainbow, D. E. Lieberman, *Nature* **2013**, 498, 483.

[17] C. D. Newton, *Textbook of Small Animal Orthopedics. London, UK: Lippincott Company* **1985**, 1101.

[18] G. Catavitello, Y. P. Ivanenko, F. Lacquaniti, *PloS one* **2015**, 10, e0133936.

[19] M. A. Lewis, M. R. Bunting, B. Salemi, H. Hoffmann, presented at Robotics and Automation (ICRA), 2011 IEEE International Conference on **2011**.

[20] Daily Mail, 2012.

[21] B. M. Kilbourne, E. Andrada, M. S. Fischer, J. A. Nyakatura, *Journal of Experimental Biology* **2016**, 219, 1405.

[22] B. Lind, H. Sihlbom, A. Nordwall, H. Malchau, *Archives of physical medicine and rehabilitation* **1989**, 70, 692.

[23] I. Toshima, H. Uematsu, T. Hirahara, *Acoustical science and technology* **2003**, 24, 327.

[24] Y. Tadesse, K. Subbarao, S. Priya, *Journal of Intelligent Material Systems and Structures* **2010**, 21, 1169.